Influence of the downstream blade sweep on cross-flow turbine performance

Abigale Snortland, Owen Williams, Brian Polagye

Abstract—**Unlike axial-flow turbines, each cycle, cross-flow turbine blades encounter a relatively undisturbed inflow for half their rotation (the "upstream sweep") and then pass through their own wake for the other half (the "downstream sweep"). While most research on cross-flow turbine optimization focuses on the power-generating upstream sweep, we observe that the downstream sweep can also significantly affect time-averaged performance. We utilize a 1-bladed cross-flow turbine to isolate the time-averaged performance contributions from the upstream and downstream sweeps. Additionally, flow fields are investigated to understand the hydrodynamic mechanisms for the observed degradation in downstream performance as tip-speed ratio increases. For this purpose, two-component, phase-locked, planar particle image velocimetry data is obtained inside the turbine swept area at two tip-speed ratios. We find that the time-averaged power generation from the upstream sweep continues to increase beyond the optimal tip-speed ratio. In contrast, the time-averaged power generation from the downstream sweep is net neutral until just before the optimal tip-ratio, after which it decreases faster than the upstream power generation increases. This indicates that the optimal tip-speed ratio is strongly influenced by the point at which the downstream sweep begins to consume appreciable power due to oppositional torque caused by high tangential blade velocities. These results highlight the importance of understanding the hydrodynamics in the downstream sweep, where induction and upstream disturbances violate the assumptions in commmon analytical models for angles of attack and relative velocity. An improved understanding of the downstream sweep may suggest strategies to improve performance and increase the optimal tip-speed ratio and performance of cross-flow turbines.**

Index Terms—**Cross-flow Turbines, Dynamic Stall, Hydrodynamics, ...**

I. Introduction

CROSS-FLOW turbines are able to harness the kinetic energy in wind, tidal currents and rivers. Relative to axial-flow turbines, cross-flow turbines may be able to achieve higher power output per unit area within an array [1]. Additional benefits include operation at lower rotation rates (reduced noise, lower risk of animal collision), operation insensitive to inflow direction (no need for active yaw control), lower blade bending stresses, simpler blade construction, ability to favorably position the generator (e.g., on the surface with floating platforms), and increased scalability [2], [3]. Because cross-flow turbines rotate perpendicular to their inflow, blades encounter a continually fluctuating angle of attack and relative inflow velocity that can lead to the unsteady, non-linear phenomenon of dynamic stall [4]–[11]. Additionally, deceleration of the flow through the turbine rotor – "induction" – is substantial, particularly for blades passing through the turbine's own wake, meaning the relative velocity and angle of attack a blade experiences during the upstream portion of its cycle differs appreciably to that of the downstream portion. These factors cause the power generated by a blade to vary throughout a single turbine rotation.

Overall, cross-flow turbine hydrodynamics and performance for a specific geometry and set of inflow parameters are functions of the blade azimuthal position, θ ($\theta = 0°$ defined as when the blade tangential velocity vector points directly upstream), and the ratio of the blade tangential velocity (the product of turbine radius and rotation rate) to the inflow velocity – the dimensionless "tip-speed ratio", λ. The upstream sweep ($\theta = 0° - 180°$) is commonly referred to as the "power stroke" of the turbine as it produces most of the hydrodynamic power, while the downstream sweep ($\theta = 180° - 360°$) is characterized by parasitic drag, post- and secondary-stall events, and boundary layer reattachment. Because of this, the relationship between the near-blade hydrodynamics and performance is relatively complicated. While multiple computational studies have investigated performance in conjunction with the near-blade hydrodynamics [5], [9], [10], [12]–[16], few [4], [7], [17] have done so experimentally. Further, While some of these works consider phase-averaged performance, to our knowledge, none have specifically partitioned and interpreted performance in the framework of upstream and downstream sweeps. In fact, most research attention to date on interpreting and optimizing cross-flow turbine performance has focused on the power-generating phase of the upstream sweep. Conversely, the focus of this paper is on the downstream sweep with an objective of illuminating a greater understanding of its importance within the broader community.

II. Methods

Here, we specifically investigate the impact of the downstream blade sweep on cross-flow turbine per-

this work was supported by the Natioanl Science Foundation Gradute Research Fellowship Program and funding from the Naval Facilities Engineering Systems Command.

A. Snortland is with the University of Washington Department of Mechanical Engineering 3900 E Stevens Way NE, Seattle, WA 98195, United States (e-mail: abigales@uw.edu).

O. Williams is with the University of Washington Department of Aeronautics and Astronautics 3940 Benton Lane NE, Seattle, WA 98195, United States (e-mail: ojhw@uw.edu).

B. Polagye is with the University of Washington Department of Mechanical Engineering 3900 E Stevens Way NE, Seattle, WA 98195, United States (e-mail: bpolagye@uw.edu).

Digital Object Identifier:
https://doi.org/10.36688/ewtec-2023-391

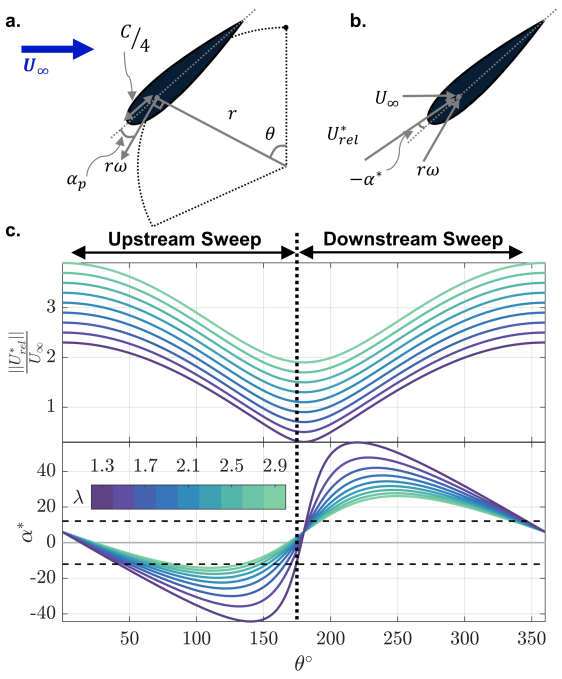

Fig. 1. (a,b) Blade geometric definitions, (c) normalized nominal relative velocity trajectories, and (d) nominal angle of attack for the two tip-speed ratios. The tangential velocity is defined tangent to the circular blade path. A positive pre-set pitch angle, α_p, is depicted in (a), and (b) shows the angle of attack definition. The static stall angle in (c) is for a foil in rectilinear flow at a similar Reynolds number ($Re_c = 1.5x10^5$, [18]). because of the rapidly varying angle of attack and appreciable induction, the comparison between α^* and the steady-state stall angle is qualitative. The vertical dashed line in (c) delineates between the upstream and downstream sweeps at $\theta = 180$.

formance using a 1-bladed turbine. Because turbine torque is measured at the center shaft in our experiments, a one-bladed turbine allows us to isolate the performance contributions for the upstream and downstream portion of the rotation (i.e., with a multi-bladed turbine, the torque contribution from each blade is ambiguous). Performance measurements are taken for a range of tip-speed ratios, $\lambda = 1.1 - 3.6$. Additionally, flow fields are investigated to contextualize the observed performance trends. For this purpose, two-component, phase-locked, planar particle image velocimetry data is obtained inside the turbine swept area at the mid-span for two tip-speed ratios, $\lambda = 1.5, 2.5$.

A. Cross-flow Turbine Theory

Two parameters often used to describe the near-blade hydrodynamics are the nominal angle of attack, α^* (affecting lift and drag coefficients), and the nominal incident relative velocity, U^*_{rel}, (affecting the magnitude of the lift and drag forces). In the absence of any induced flow (i.e., proximate changes in streamwise and cross-stream velocities as a consequence of interaction with the blade), the nominal angle of attack, defined as the angle between the chord line and U^*_{rel} at the quarter chord, $c/4$, is

$$\alpha^*(\lambda,\theta) = -tan^{-1}\left[\frac{sin(\theta)}{\lambda + cos(\theta)}\right] + \alpha_p \qquad (1)$$

where α_p is the blade preset pitch angle, θ is the blade azimuthal position ($\theta = 0°$ defined as when the turbine blade faces directly upstream), and λ is the tip-speed ratio. The latter is a non-dimensional representation of the turbine rotation rate, defined as

$$\lambda = \frac{r\omega}{U_\infty} \qquad (2)$$

where r is the turbine radius and ω is the rotation rate. The nominal incident velocity (relative velocity to $c/4$) is the vector sum of the tangential velocity, $r\omega$, and the freestream velocity, U_∞, such that its non-dimensional magnitude is

$$\frac{||U^*_{rel}(\lambda,\theta)||}{U_\infty} = \sqrt{\lambda^2 + 2\lambda cos(\theta) + 1}). \qquad (3)$$

We refer to these as nominal quantities because deceleration of the flow through the turbine rotor (induction) is appreciable but unknown.

Because α^* and U^*_{rel} depend on λ, the phase, duration, and severity of dynamic stall are influenced by this parameter. A schematic of the blade geometry and azimuthal variations in $||U^*_{rel}||$ and α^* over one turbine rotation is shown in Fig. 1. For negative α^*, on the upstream sweep, the lift vector points inward to the center of rotation and, therefore, the suction side of the blade is the inner surface. Conversely, for positive α^* on the downstream sweep, the suction side of the blade is the outer surface. A decrease in λ reduces $||U^*_{rel}||$ and increases the range of α^* encountered during a cycle, which corresponds to earlier vortex shedding, increased stall severity, and delayed flow recovery. In severe, or "deep" dynamic stall cases (lower λ, larger α ranges), the near-blade flow field is characterized by the formation and roll-up of an energetic dynamic stall vortex that is on the order of the blade chord. After shedding, the blade experiences a sharp drop-off in lift production and an increase in drag and prolonged flow separation. In contrast, any vortex growth in "light" dynamic stall cases (higher λ, smaller α ranges) is prematurely terminated, prior to it reaching is greatest strength, and the flow is able to recover faster relative to deep dynamic stall [19], [20].

B. Experimental Facility

Experiments were performed in the Alice C. Tyler flume at the University of Washington, a rendering of which is shown in Figure 2a. The data presented in this paper utilized a mean dynamic water depth, h, of 0.52 m, resulting in a channel cross-sectional area A_C of 0.39 m^2 (0.75 m width). The water temperature was maintained at 39 ± 0.2 °C, giving a ρ of 993 kg/m^3, and a kinematic viscosity, ν, of $6.7x10^{-7}$ m^2/s. An acoustic Doppler velocimeter (Nortek Vectrino) operating at a 100 Hz sampling rate and positioned approximately 5 diameters upstream of the turbine rotor, measured an average U_∞ of 0.9 m/s with a turbulence intensity, TI, of 1-2% . These conditions corresponded to a depth-based Froude number, $Fr = \frac{U_\infty}{\sqrt{gh}}$, of 0.4 where the gravitational constant g is 9.81 m/s^2.

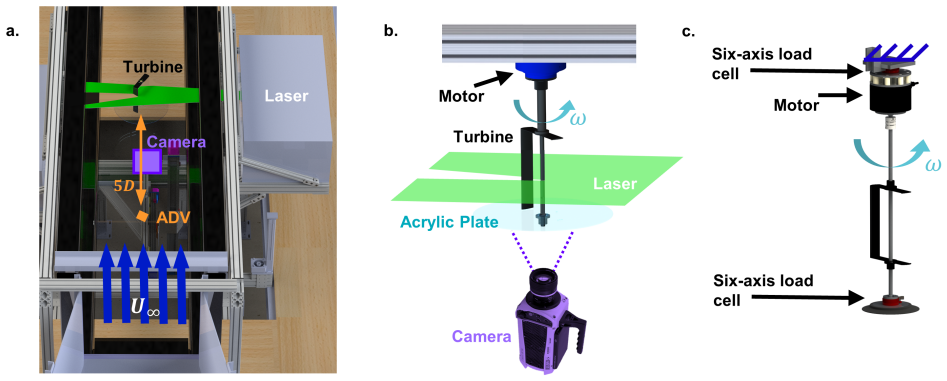

Fig. 2. (a) Annotated PIV and performance experimental setup in the flume, (b) "PIV measurement" test rig with the with camera and laser sheet arrangement, and (c) "performance measurement" test rig.

1) Cross-flow turbine and test rigs: Two experimental test rigs are used in these experiments. The "PIV measurement" test rig is shown in Figure 2b, and the "performance measurement" test rig is shown in Figure 2c. In either configuration, turbine rotation rate, ω is held constant by a servomotor. Blade position is measured by the servomotor encoder with a resolution of 2^{18} counts/rotation and ω is estimated by differentiation. MATLAB Simulink Desktop Real-Time is used for data collection and turbine control. For each control set point (i.e., a single ω), all data are acquired for 60 seconds at 1 kHz. Experiments utilize a one-bladed (NACA 0018 foil) turbine. The turbine has a radius of 8.6 cm, blade span of 23.4 cm, a blade chord length, C, of 4.06 cm and a 6° preset pitch. The blockage ratio, $\beta = \frac{2Lr}{A_C}$ is 10.3% and the Reynolds number, $Re_c = \frac{U_\infty c}{\nu}$ is $5.5x10^4$. While our Reynolds number is lower and our blockage is higher than what may be expected for full-scale operation, these experiments enable the study of the fundamental dynamics of cross-flow turbine operation.

"PIV measurements" test rig: The "PIV measurement" test rig utilizes a Yaskawa SGMCS-02B servomotor rigidly coupled to the flume cross beam. In this configuration, no forces are measured during the PIV acquisition. To facilitate PIV imaging of streamwise planes along the blade-span from cameras positioned below the flume, the turbine is constructed with a 40 cm diameter (2.3x turbine diameter) acrylic plate at the bottom and a NACA 0008 foil strut at the top. The plate is intentionally oversized so that the index of refraction is constant across the field of view. This turbine, however, is sub-optimal for performance measurements (specifically at high rotation rates). Additional details are provided in [21].

"Performance measurement" test rig: Forces and torques are measured by a pair of six-axis reaction load cells (above rotor: ATI Mini45, below rotor: ATI Mini40) and the turbine is controlled with a Yaskawa SGDV-2R1F01A002 drive. Additional details are provided in [22]. To improve performance measurements, this turbine is comprised of NACA 0008 foil struts supporting each end of the blade span. Since the turbine support structure incurs an appreciable parasitic torque from the struts and turbine shaft, blade-level performance is isolated by subtracting phase-averaged performance for the turbine support structure (blade removed, at the same operating conditions) from the full turbine performance measurements. We note that this relies on an assumption that secondary interactions between the blades and support structures are minimal, which has been confirmed by prior work [23], [24]. All torque measurements were filtered with a low-pass, zero-phase, Butterworth filter to remove high-frequency electromagnetic interference from the servomotor. The 30 Hz cutoff frequencies used for the turbine and support structure force data are more than 10 harmonics faster than the blade passage frequency and the filter is unlikely to remove any hydrodynamic forcing.

Through a turbine rotation, the hydrodynamic power, P, is non-dimensionalized as the coefficient of performance, C_P. This is defined as

$$C_P(\lambda,\theta) = \frac{P(\theta)}{\rho U_\infty^3 Lr} \tag{4}$$

where ρ is fluid density and L is the blade span. The hydrodynamic torque, Q, is non-dimensionalized as

$$C_Q(\lambda,\theta) = \frac{Q(\theta)}{\rho U_\infty^2 Lr^2}. \tag{5}$$

The torque and performance coefficients are directly related by the tip-speed ratio as

$$C_P = C_Q\lambda. \tag{6}$$

Time-averages of any quantity, X, are represented as $\overline{X}$. The overall time-average is an average of the entire time-series for a single λ, truncated to an integer number of rotations. We also present time averages conditional on θ. For example, the upstream time-averaged performance coefficient is computed by averaging all of the data points in the time-series that were measured between $\theta = 0°$ and $\theta = 180°$. A corresponding calculation is used to define a time-averaged downstream performance coefficient. Phase

averages of any quantity X are represented as $\langle X \rangle$. The phase average is an average for a single azimuthal position across multiple cycles with constant λ. Since the performance data is captured continuously, we utilize a 1° θ bin for phase-averaging.

C. PIV Measurement

Two-dimensional, two-component, phase-locked, flow-field measurements were obtained in a streamwise plane at the mid-span of the turbine. PIV acquisition was controlled by TSI Insight and acquisition for each cycle commenced upon receipt of trigger pulses sent at a specified θ from the Simulink model controlling the turbine.

The general arrangement of the PIV laser and cameras is shown in Figure 2a. A dual cavity, Nd:YLF laser (Continuum Terra PIV) illuminated the flow with an approximately 2 mm thick light sheet in the field of view, FoV. A high-speed camera (Vision Research Phantom v641) with 2560 x 1600 resolution acquired images. Three PIV setups were utilized in this work. The first two, "wide" and the "narrow" utilized a horizontal laser sheet in the cross-stream direction while the "angled" case utilized a horizontal laser sheet angled with respect to the cross-stream direction to capture portions of the cycle that were otherwise blocked by shadows from the turbine blade and support structure. The "wide" setup utilized a 60 mm lens at f#16. The calibration was 7.9 pixels/mm producing a FoV of 32.4 x 20.3 cm [$8c$ ($1.9D$) x $5c$ ($1.2D$)]. The "narrow" setup utilized a 135 mm lens at f#16. The calibration was 12.6 pixels/mm producing a FoV of 20.3 x 12.7 cm [$5c$ ($1.2D$) x $3.1c$ ($0.74D$)]. The "angled" setup utilized a 135 mm lens at f#16. The calibration was 10 pixels/mm producing a FoV size in between that of the "wide" and "narrow" setups of 25.6 x 16 cm [$6.3c$ ($1.5D$) x $3.9c$ ($0.93D$)]. FoV positioning relied on a combination of camera and turbine movement. A motorized, three-axis gantry positioned the camera relative to the laser sheet and provided the dominant adjustment for cross-stream FoV positioning, as well as fine adjustments in the streamwise direction. The size of the FoVs for the "narrow" and "angled" setups were smaller then the turbine diameter, so PIV data were acquired at multiple cross-stream camera locations to capture the whole turbine rotation. A calibration was taken for each camera location. The limited streamwise extent of the laser sheet necessitated shifting the turbine by $\approx \frac{1}{2}D$ upstream to illuminate and capture the downstream blade sweep (logistically preferred to shifting the laser).

Sequences of 59 image pairs for the "wide" setup, and 15 image pairs for the "narrow" and "angled" setups were acquired per rotational cycle with prescribed angular displacements between frames ranging between approximately 3 and 5°, depending on desired phase resolution. 20 images pairs were captured at each phase for the "wide" setup and 85 for the "narrow" and "angled" setups. The flow seeding (10 μm hollow-glass beads) produced particle images of approximately 3 pixels in diameter. To minimize laser reflections at the blade surface, matte black paint was applied. PIV processing was performed in LaVision DaVis (version 10.1.1) and post-processing and data visualization were done in MATLAB. Background subtraction using a Butterworth filter on phase-matched images mitigated residual reflections and background illumination variation. The shadowed regions, visible turbine structures, and remaining reflections were manually masked prior to PIV processing. Processing utilized a multi-grid, multi-pass cross-correlation algorithm with adaptive image deformation, resulting in final window sizes of 32 x 32 pixels with a 75% overlap.

Both the turbine shaft and blade cast shadows in the laser sheet. Therefore, to obtain data adjacent to the suction and/or pressure sides of the foil at all phases of interest, PIV measurements were conducted with the turbine spinning in both clockwise and counter-clockwise directions. Both rotation directions were combined into composite fields in post processing. This was done by first determining the center of rotation, as described in [21]. The phase-averaged flow fields were then interpolated to a common grid and the two rotation directions at each phase for the same FoV were averaged. In this way, the influence of the shadows is minimized.

The flow field analysis in this work utilizes either global time-averaged horizontal velocity magnitude fields, $||\overline{\vec{V}}||$, or phase-averaged relative velocity fields in the blade-centric reference frame, ($||\langle U_{rel} \rangle||$). Here the $||$ $||$ denote the magnitude. The $||\overline{\vec{V}}||$ fields are computed separately for the upstream and downstream sweeps and are an average of all the composite fields from the "wide" data set. Any regions of missing data in the composite fields (regions that are in the masked areas in both rotation directions) are set to NaN and ignored in the time-average. While this is is not a true time average since the data is phase locked, the phase separation is small for the "wide" cases, 3°, and all phases are weighted equally in the average. The ($||\langle U_{rel} \rangle||$) fields are computed using the composite "narrow" and "angled" fields following the process laid out in [21].

III. Results

A. Performance and Torque Measurements

The characteristic time-averaged performance curve presented in Fig. 3 highlights the dependency of turbine performance on the tip-speed ratio. Overall turbine performance increases up until a certain optimal tip-speed ratio ($\lambda = 2.8$) beyond which performance begins to decrease. Most research attention to date has interpreted the mechanisms behind this optimal performance condition in the context of the power-generating phases of the "upstream sweep". However, when the upstream and downstream time-averaged performance are partitioned, as in Fig. 3, it is clear the performance in the upstream sweep continues to increase beyond the optimal tip-speed ratio. In contrast, the performance in the downstream sweep is net neutral (i.e., $C_P \approx 0$ when averaged over the downstream sweep) until around $\lambda = 2.5$ where

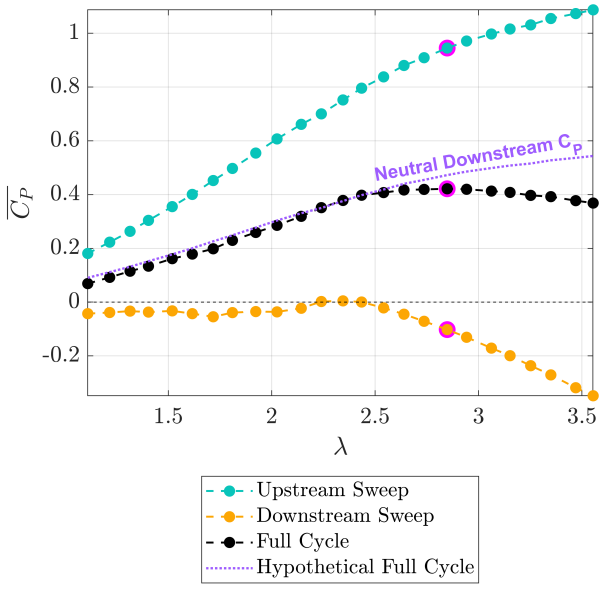

Fig. 3. Time-averaged coefficient of performance. The black line is the characteristic time-averaged performance curve (time-average over the full cycle). The teal line is the time average of performance data for just the upstream sweep ($\theta = 0° - 180°$). Similarly, the yellow curve is the time-average of performance data for just the downstream sweep ($\theta = 180° - 360°$). The purple dotted line represents a hypothetical case for full cycle performance using actual upstream sweep performance and neutral downstream performance (i.e., $C_P = 0$). The points outlined in magenta correspond to the optimal tip-speed ratio.

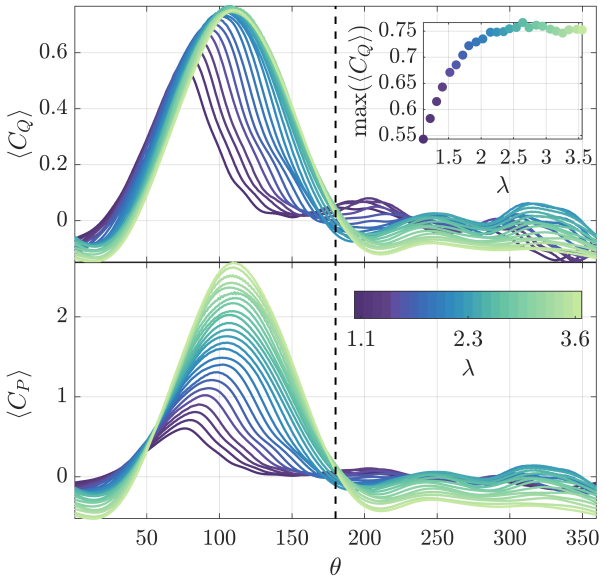

Fig. 4. (Top) Phase-averaged coefficient of torque (bottom) and coefficient of performance. The inset is the value of the maximum coefficient of torque with tip-speed ratio. The vertical dashed line represents the delineation between the upstream and downstream sweeps.

it begins to decrease at a faster rate than the upstream performance increases. This indicates that the optimal tip-speed ratio is strongly influenced by the degradation in the downstream performance. This is further highlighted by a hypothetical case of neutral downstream performance which indicates that performance would continue to increase with tip-speed ratio over the range tested if the downstream performance remained neutral at the high tip-speed ratios.

To further investigate the contributions of the upstream and downstream blade sweeps, we present the phase-averaged coefficient of torque and power/performance in Fig. 4. As the tip-speed ratio increases, the nominal angle of attack range experienced by the blade decreases (Fig. 1), dynamic stall weakens, and the relative velocity incident on the blade increases. In aggregate, this increases the amplitude of the torque peak in the upstream sweep and shifts that peak later in the cycle until the timing and amplitude of the peak becomes independent of λ around $\lambda = 2.5$ (Fig. 4 inset). Therefore, the increased phase-average performance at high tip-speed ratios in the upstream sweep (Fig. 4 bottom) is primarily the result of the multiplication of torque with the higher tip-speed ratio (Eq. 4) and not higher hydrodynamic force production by the blades. In contrast, parasitic torque becomes increasingly detrimental in the downstream sweep at higher tip-speed ratios. While the degradation in downstream performance appears subtle, it dominates over the performance gains in the upstream sweep.

B. Flow Fields

To better understand the hydrodynamic mechanisms underlying performance in the downstream sweep, flow fields are analyzed for two cases (one with lower performance, $\lambda = 1.5$, and one near-optimal $\lambda = 2.5$). The flow field with lower performance is relevant to turbine operation when "underspeed" control is used to shed power above rated speed. The $\lambda = 1.5$ case experiences deep dynamic stall, while the $\lambda = 2.5$ experiences light dynamic stall. The $\lambda = 2.5$ case is slightly less than optimal ($\lambda = 2.8$) and corresponds to the point where the downstream performance switches from being consistently nearly net-neutral to decreasing monotonically.

The large differences in performance and torque production between the upstream and downstream sweeps is primarily a consequence of deceleration of the flow through the turbine due to momentum extraction. The inflow velocity alteration through the rotor and near-wake is termed "induction" and is accompanied by flow field acceleration around the rotor. For all tip-speed ratios, performance and torque production are at a minimum during the downstream sweep, in part due to lower incident velocities. The magnitude of induction differs between the upstream and downstream sweeps and with tip-speed ratio, as highlighted in the time-averaged flow fields in Fig. 5. The higher tip-speed ratio case, $\lambda = 2.5$, exhibits lower in-rotor velocities during both the upstream and downstream sweeps with the most pronounced deceleration in the downstream sweep and near-wake. The higher average velocity region for the $\lambda = 1.5$ case between $\theta = 90° - 180°$ is a signature of the strong dynamic stall vortex while the blade is in that region.

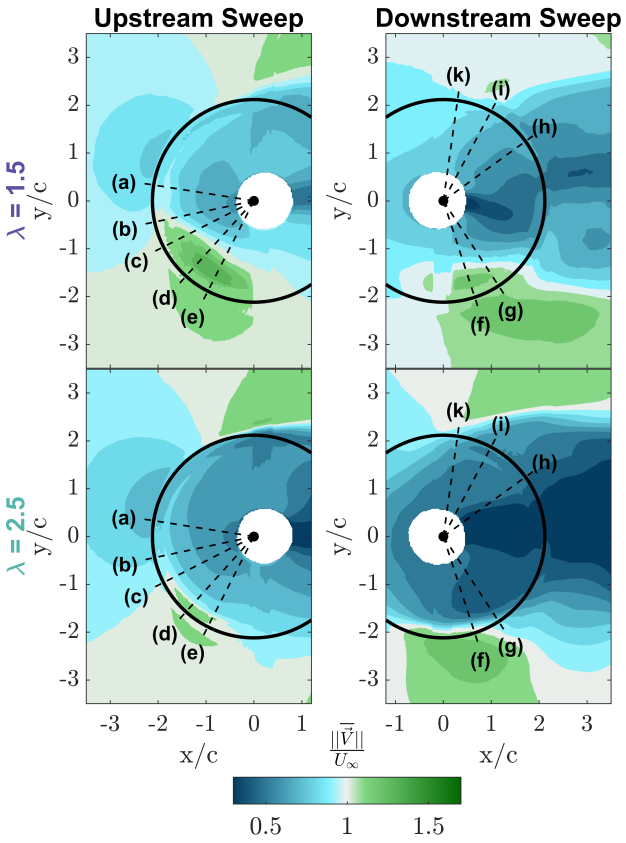

Fig. 5. Time-averaged horizontal velocity magnitude fields for the upstream and downstream sweeps. The black circles represent the blade sweep. The radial dashed lines correspond to the locations of the phase-averaged flow fields presented in Figs. 7 and 8. The upstream sweep is averaged over $\theta = 9° : 3° : 176°$ and the downstream sweep is averaged over $\theta = 183° : 3° : 353°$.

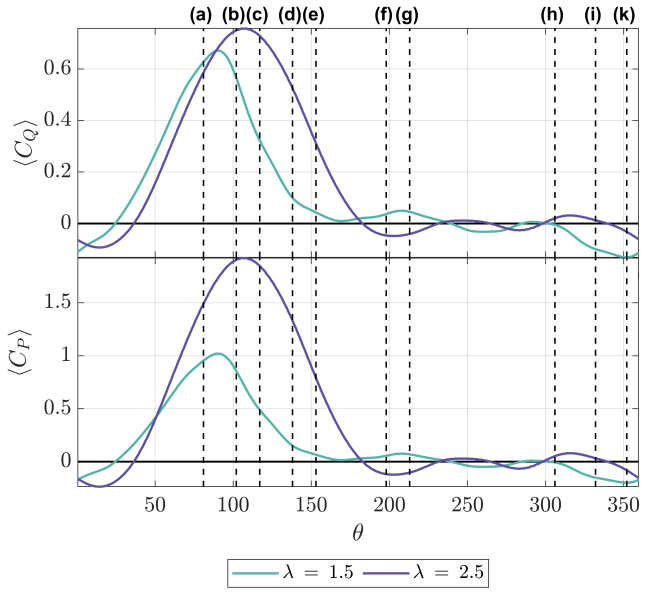

Fig. 6. Select phase-averaged torque (top) and performance (bottom) trajectories corresponding to tip-speed ratios with PIV data. The black horizontal lines differentiate between positive and negative regions of torque and performance. The vertical dashed lines correspond to the locations of the phase-averaged flow fields presented in Figs. 7 and 8.

We also observe velocities $\geq U_\infty$ in the bypass region between the turbine and the flume walls as a result of the divergence of the flow around the turbine.

To investigate this effect on the hydrodynamics, we consider the phase-averaged flow fields in the downstream sweep. Select phase-averaged performance and relative velocity fields for the upstream and downstream sweeps are presented in Figs. 6-8. In qualitative agreement with prior experiments [4], [7], [9], [21] and simulations [5], [15], the near-blade hydrodynamics depend strongly on the tip-speed ratio and differ substantially between the upstream (Fig. 7) and downstream (Fig. 8) portions of the rotation. Overall, dynamic stall severity and turbine performance are inversely proportional for the two cases. The higher tip-speed ratio case clearly decreases stall severity, as evidenced by the limited coherent structures, and has correspondingly higher performance. Because the lower tip-speed ratio leads to a wider oscillation in angle of attack, the $\lambda = 1.5$ case experiences deep dynamic stall. This is evidenced by the roll-up (Fig. 7c) and shedding (d-e) of the strong dynamic stall vortex, as well as prolonged post-stall flow separation (Fig. 8f-g) and more persistent separated flow during the downstream sweep (h-k). This more severe dynamic stall process corresponds to a smaller amplitude performance peak which occurs earlier in the cycle in comparison to the $\lambda = 2.5$ case. In contrast, for $\lambda = 2.5$, the foil experiences only light dynamic stall with smaller vortex structures, limited flow separation (a-e), and faster post-stall flow recovery (f-k). Despite the higher induction evident for the $\lambda = 2.5$ case, it is clear that the relative velocities around the blade in the upstream and downstream sweeps are higher. This is because the higher tangential blade velocity for $\lambda = 2.5$ outweighs the reduction in inflow velocity from induction.

While the hydrodynamic differences in the upstream sweep are in line with dynamic stall theory and qualitatively explanatory of the increased performance for the $\lambda = 2.5$ case, the downstream sweep exhibits clear differences in the near-blade hydrodynamics (albeit less dramatic) despite the time-averaged performance in the downstream region being nearly identical for both tip-speed ratios (Fig. 3). In line with the deeper stall experienced during the upstream sweep, the $\lambda = 1.5$ case exhibits more substantial flow separation during the entirety of the downstream sweep in comparison to the $\lambda = 2.5$ case. However, at the beginning of the downstream sweep, after the suction and pressure sides of blades have switched, we observe higher torque and performance coefficients for $\lambda = 1.5$ (f-g). Here, the shed dynamic stall vortex remains near the blade and the relative velocities around the blade (particularly the suction side) are approaching zero, yet the blade still produces some torque, indicating beneficial secondary stall hydrodynamics. In contrast, the $\lambda = 2.5$ case exhibits regions of recirculating flow leftover from the upstream sweep, on what is now the pressure side of the blade at the trailing edge, and experiences higher relative velocities in comparison to the $\lambda = 1.5$ case. This results in parasitic (negative) torque. During the middle of the downstream sweep

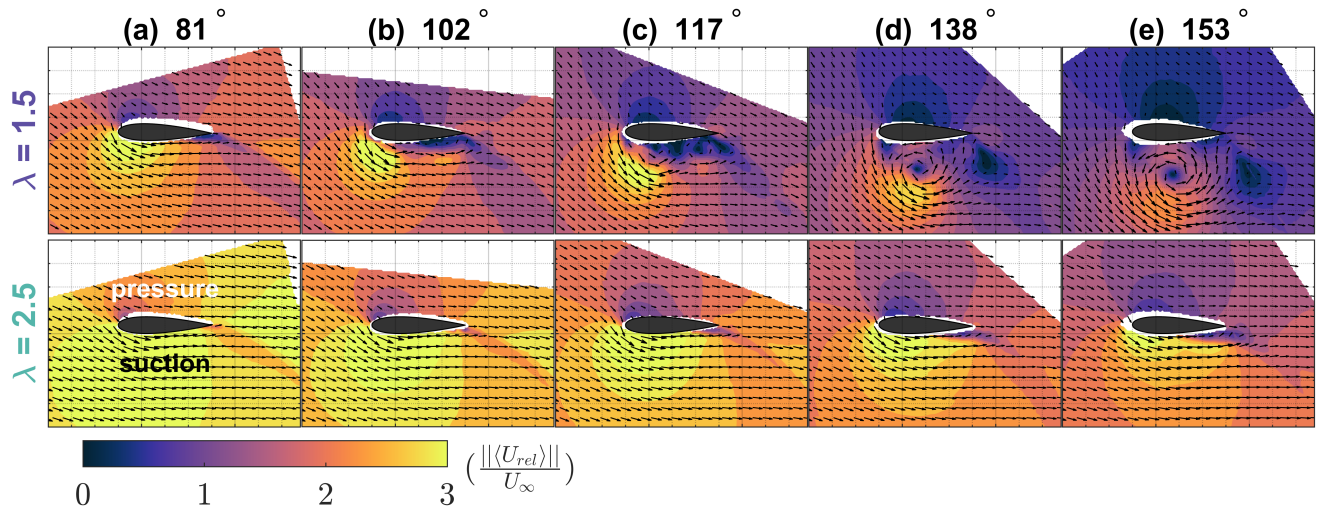

Fig. 7. Upstream phase-averaged relative velocity fields at select phases for both tip-speed ratios. Every 5^{th} velocity vector is plotted. The axis grid spacing is $c/4$. The colormap is from [25]

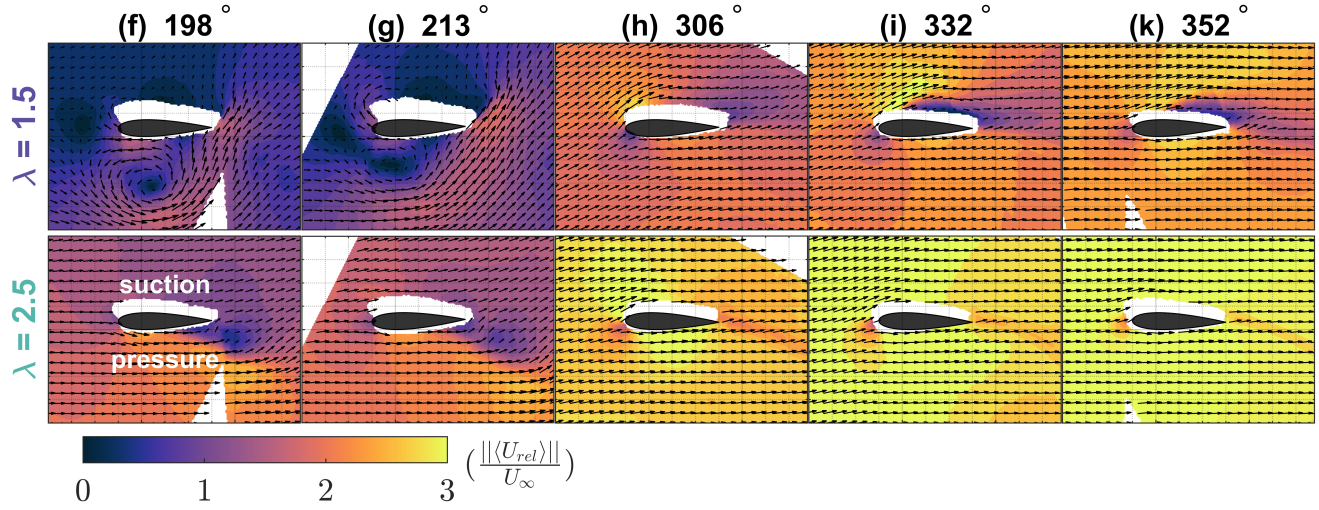

Fig. 8. Downstream phase-averaged relative velocity fields at select phases for both tip-speed ratios. Every 5^{th} velocity vector is plotted. The axis grid spacing is $c/4$. The colormap is from [25]

($\theta = 225° - 300°$) both tip-speed ratios have near-zero torque coefficients. At the end of the downstream sweep, the torque benefit for $\lambda = 1.5$ at the beginning of the downstream sweep is counteracted by parasitic torque in (h-k), where significant flow separation is visible and the relative velocities increase as the blade encounters the higher velocity bypass flow. In this region, the $\lambda = 2.5$ case produces a small amount of torque (h-i) before drag dominates as the blades enter the higher velocity bypass flow. For both cases, the parasitic torque at the end of the downstream sweep continues into the beginning of the upstream sweep. Overall, both tip-speed ratio cases exhibit opposing behaviors (where one case produces torque the other consumes torque) and oscillate between positive and negative torque and performance in the downstream sweep, resulting in nearly net neutral time-averaged performance in this region.

IV. Discussion

The flow field cases highlighted here indicate a trend towards more attached flow in the downstream sweep as the tip-speed ratio increases. While these experiments did not include any tip-speed ratio cases beyond $\lambda = 2.5$ where the downstream sweep becomes increasingly detrimental, it is expected that those cases would converge towards increasingly attached flow in the downstream sweep. This is because the nominal angle of attack profiles converge towards the preset pitch angle at high tip-speed ratios (Eq. 1). An increase in attached flow is normally indicative of a decrease in drag (less negative torque production), however, the downstream performance decreases at a nearly linear rate beyond $\lambda = 2.5$. This contradiction is likely explained by the relative velocity magnitude and its angle in relation to the direction of rotation.

The relative velocity incident on the blade throughout the turbine rotation is the vector sum of the in-rotor flow velocity encountered by the blade (influenced by induction and shed fluid structures) and the tangential velocity of the blade. The blade tangential velocity increases continuously with tip-speed ratio and, even in the absence of induction, the relative velocities will converge towards the tangential velocity

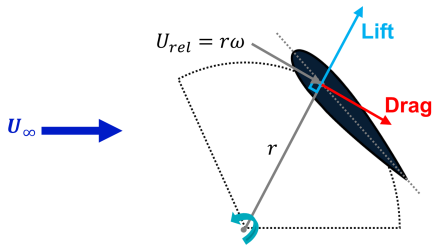

Fig. 9. Blade level force schematic highlighting the directions of lift and drag for the limiting case where the relative velocity is equal to the blade tangential velocity.

at sufficiently high tip-speed ratios. For this limiting case, even if there is favorable lift production, the lift force vector is perpendicular to the rotation direction (Fig. 9) and, therefore, does not produce any force in the direction of blade rotation. Similarly, even for low drag coefficients associated with fully attached flow, the drag force directly opposes the rotation direction and increases with tangential velocity. It is well known that in-rotor velocities decrease at higher tip-speed ratios as more flow is diverted around the turbine due to induction. As induction increases, the accuracy of the nominal formulations for the relative velocity and angle of attack decreases, and the actual angle of attack and relative velocities will converge to the limiting case at earlier tip-speed ratios. This is because the contribution of the inflow velocity is diminished and the tangential velocity dominates. We see this effect in the phase-averaged torque coefficient (Fig. 4) where the torque contribution in the downstream sweep becomes increasingly constant and detrimental beyond $\lambda = 2.5$ due to the high blade tangential velocities and increased induction. At high tip-speed ratios, the mechanisms to increase performance in the downstream sweep are to (1) reduce induction (increasing the tip-speed ratio at which lift no longer contributes to torque), (2) entrain flow or momentum into the rotor (3) reduce the drag coefficient, or (4) reduce the tangential velocity. As shown by the hypothetical case of neutral downstream performance in Fig. 3, we can improve overall turbine performance, even if it is not possible to produce power in the downstream sweep, by reducing the parasitic torque.

V. Conclusion

To date, most research on contextualizing optimal turbine performance has focused on the hydrodynamics of the upstream blade sweep, where most of the power is produced. In this work, we utilize turbine performance and torque measurements in concert with phase-locked PIV flow fields to highlight the influence of the downstream sweep. Performance and torque measurements are presented for $\lambda = 1.1 - 3.6$ and flow fields are presented for a poor-performing case, $\lambda = 1.5$, and a well-performing case, $\lambda = 2.5$. The use of a 1-bladed turbine allowed for independent analysis of performance and torque contributions between the upstream and downstream blade sweeps.

Overall, the time-averaged performance in the upstream sweep continues to increase beyond the optimal tip-speed ratio, $\lambda = 2.8$. In contrast, time-averaged performance in the downstream sweep is net neutral (i.e., $C_P \approx 0$) until $\lambda = 2.5$ where it begins to decrease at a faster rate than the upstream performance increases. This indicates that the optimal tip-speed ratio is strongly influenced by the point at which the downstream sweep begins to consume appreciable power. Torque production converges with increased tip-speed ratio during the upstream sweep while parasitic torque becomes more detrimental in the downstream sweep. Therefore, the increased performance at high tip-speed ratios in the upstream sweep is primarily the result of the increased tip-speed ratio (higher ω) and not higher torque coefficients.

Flow field measurements suggest an increase in, and faster, flow attachment during the downstream sweep at higher tip-speed ratios, an observation that is normally associated with reduced drag. Instead, we observe increasingly detrimental parasitic torque. This contradiction is explained by the influence of the relative velocity incident of the blade. At high tip-speed ratios, significant flow deceleration through the turbine rotor (induction) contributes to a convergence in the relative velocity to the blade tangential velocity. This, in turn, results in diminished beneficial torque from lift production and higher parasitic drag in the downstream sweep. This drag increase results in the observed torque and performance degradation beyond $\lambda = 2.5$, and highlights the importance of understanding the role of the downstream sweep in overall turbine performance.

Acknowledgement

The authors thank the Alice C. Tyler Charitable Trust for supporting the research facility and acknowledge the substantial contributions by Benjamin Strom, Hannah Ross, Aidan Hunt, Carl Stringer, Erik Skeel, and Craig Hill for their contributions to the development and upgrades of the experimental setup and code base. We also thank our colleagues in the Pacific Marine Energy Center for their continued support.

References

[1] J. O. Dabiri, "Potential order-of-magnitude enhancement of wind farm power density via counter-rotating vertical-axis wind turbine arrays," *Journal of Renewable and Sustainable Energy*, vol. 3, no. 4, pp. 1–12, 2011.

[2] M. Mahmood, N. Hayat, A. U. Farooq, Z. Ali, S. R. Jamil, and Z. Hussain, "Vertical axis wind turbine – a review of various configurations and design techniques," *Renewable and Sustainable Energy Reviews*, vol. 16, no. 4, pp. 1926 – 1939, 2012.

[3] S. Eriksson, H. Bernhoff, and M. Leijon, "Evaluation of different turbine concepts for wind power," *Renewable and Sustainable Energy Reviews*, vol. 12, no. 5, pp. 1419 – 1434, 2008.

[4] A. Snortland, O. Williams, and B. Polagye, "Influence of near-blade hydrodynamics on cross-flow turbine performance," *Proceedings of the 13th European Wave and Tidal Energy Conference*, pp. 1 – 9, 2019.

[5] M. Dave, B. Strom, A. Snortland, O. Williams, B. Polagye, and J. A. Franck, "Simulations of intracycle angular velocity control for a crossflow turbine," *AIAA Journal*, vol. 59, no. 3, pp. 812–824, mar 2021.

[6] M. Dave and J. A. Franck, "Comparison of rans and les for a cross-flow turbine in confined and unconfined flow," *Journal of Renewable and Sustainable Energy*, vol. 13, no. 6, p. 064503, 2021.

[7] S. Le Fouest and K. Mulleners, "The dynamic stall dilemma for vertical-axis wind turbines," *Renewable Energy*, vol. 198, pp. 505–520, 2022.
[8] A. Bianchini, F. Balduzzi, F. Ferrara, and L. Ferrari, "Virtual incidence effect on rotating airfoils in darrieus wind turbines," *Energy Conversion and Management*, vol. 111, pp. 329 – 338, 2016.
[9] C. Simão Ferreira, G. Van Kuik, G. Van Bussel, and F. Scarano, "Visualization by PIV of dynamic stall on a vertical axis wind turbine," *Experiments in Fluids*, vol. 46, no. 1, pp. 97–108, 2009.
[10] A.-J. Buchner, M. W. Lohry, L. Martinelli, J. Soria, and A. J. Smits, "Dynamic stall in vertical axis wind turbines: Comparing experiments and computations," *Journal of Wind Engineering and Industrial Aerodynamics*, vol. 146, pp. 163 – 171, 2015.
[11] R. Dunne and B. McKeon, "Dynamic stall on a pitching and surging airfoil," *Experiments in Fluids*, vol. 56, 08 2015.
[12] N. Fujisawa and S. Shibuya, "Observations of dynamic stall on turbine blades," *Journal of Wind Engineering and Industrial Aerodynamics*, vol. 89, no. 2, pp. 201–214, 2001.
[13] J. M. Edwards, L. Angelo Danao, and R. J. Howell, "Novel experimental power curve determination and computational methods for the performance analysis of vertical axis wind turbines," *ASME. J. Sol. Energy Eng.*, vol. 134, no. 4, 2012.
[14] A. Rezaeiha, H. Montazeri, and B. Blocken, "Characterization of aerodynamic performance of vertical axis wind turbines: Impact of operational parameters," *Energy Conversion and Management*, vol. 169, pp. 45 – 77, 2018.
[15] H.-C. Tsai and T. Colonius, "Coriolis effect on dynamic stall in a vertical axis wind turbine," *AIAA Journal*, vol. 54, no. 1, pp. 216–226, 2016.
[16] K. Almohammadi, D. Ingham, L. Ma, and M. Pourkashanian, "Modeling dynamic stall of a straight blade vertical axis wind turbine," *Journal of Fluids and Structures*, vol. 57, pp. 144–158, 2015. [Online]. Available: https://www.sciencedirect.com/science/article/pii/S0889974615001334
[17] S. Le Fouest, D. Bensason, and K. Mulleners, *Asymmetry of timescales, loads, and flow structures for a vertical-axis wind turbine blade*, 2022.
[18] W. Timmer, "Two-dimensional low-reynolds number wind tunnel results for airfoil naca 0018," *Wind engineering 32(6), 525-537*, vol. 32, 12 2008.
[19] K. Mulleners and M. Raffel, "The onset of dynamic stall revisited," *Exp Fluids*, vol. 52, pp. 779 – 793, 2012.
[20] W. J. McCroskey, "The Phenomenon of Dynamic Stall," 1981.
[21] A. Snortland, I. Scherl, B. Polagye, and O. Williams, "Cycle-to-cycle variations in cross-flow turbine performance and flow fields," *arXiv preprint arXiv:2302.03218*, 2023.
[22] B. Polagye, B. Strom, H. Ross, D. Forbush, and R. J. Cavagnaro, "Comparison of cross-flow turbine performance under torque-regulated and speed-regulated control," *Journal of Renewable and Sustainable Energy*, vol. 11, no. 4, p. 044501, 2019.
[23] B. Strom, N. Johnson, and B. Polagye, "Impact of blade mounting structures on cross-flow turbine performance," *Journal of Renewable and Sustainable Energy*, vol. 10, no. 3, p. 034504, 2018.
[24] A. Hunt, C. Stringer, and B. Polagye, "Effect of aspect ratio on cross-flow turbine performance," *Journal of Renewable and Sustainable Energy*, vol. 12, no. 5, p. 054501, 2020.
[25] K. M. Thyng, C. A. Greene, R. D. Hetland, H. M. Zimmerle, and S. F. DiMarco, "True colors of oceanography: Guidelines for effective and accurate colormap selection," *Oceanography*, September 2016. [Online]. Available: https://doi.org/10.5670/oceanog.2016.66